Chapter 2
Photometric Properties of Solar System Ices

A.J. Verbiscer, P. Helfenstein, and B.J. Buratti

Abstract We present an overview of fundamental photometric properties of icy surfaces throughout the Solar System and investigate the extent to which these properties reflect the evolution of the bodies on which they reside. We review photometric models and their parameters and discuss the physical interpretability of those parameters. We focus on those fundamental photometric properties, primarily albedo and the near-opposition phase function, which are independent of any interpretation from the application of a photometric model. Finally, we offer suggestions for future work, both observational and laboratory measurements, which will enhance the scientific return from continued photometric studies of icy bodies in the Solar System.

2.1 Introduction

Planetary photometry is the quantitative measurement of reflected and emitted radiation from solar system bodies. Over the past three decades, the observational data set of icy planetary surfaces has expanded considerably. Spacecraft imaging systems have returned hundreds of thousands of multi-wavelength images of giant planet satellites, rings, and even comet nuclei. These platforms have delivered spatial resolutions and access to viewing geometries unattainable from Earth. In addition, the advent of larger aperture ground-based telescopes combined with advances in detector technology

A.J. Verbiscer (✉)
Department of Astronomy, University of Virginia, Charlottesville, VA, USA
e-mail: verbiscer@virginia.edu

P. Helfenstein
Department of Astronomy and Space Sciences, Cornell University, Ithaca, NY, USA
e-mail: helfenstein@astro.cornell.edu

B.J. Buratti
Jet Propulsion Laboratory, California Institute of Technology, Pasadena, CA, USA
e-mail: buratti@jpl.nasa.gov

M.S. Gudipati and J. Castillo-Rogez (eds.), *The Science of Solar System Ices*,
Astrophysics and Space Science Library 356, DOI 10.1007/978-1-4614-3076-6_2,

have yielded photometric measurements (albedo, color, and phase function) from an entirely new classification of icy bodies, the transneptunian objects (TNOs), and an expanded collection of irregular satellites and Jupiter and Neptune Trojan asteroids.

An important goal of planetary photometry is to infer physical surface properties from the variation in the intensity of reflected sunlight as a function of illumination and viewing geometry. Physically motivated photometric models relate this behavior to properties such as roughness, particle structure, and compaction state. This technique is a valuable means of discerning surface characteristics even on scales below the resolution limit of the telescopes observing them. In general, robust estimates of surface properties from photometric analyses require observations which span the broadest possible range of viewing and illumination angles. Although the size of the Earth's orbit restricts this range for ground-based observations, surface characteristics of objects not visited by spacecraft can be inferred from similarities between the photometric properties of those bodies for which spacecraft observations do exist. Thus spacecraft images provide not only photometric measurements of their direct targets but they may also supply context for similarly classified objects.

Since the last review of the photometric properties of ices in the Solar System (Verbiscer and Helfenstein 1998) several advances in photometric models have improved our ability to reproduce the scattering behavior exhibited by planetary surfaces. For example, models available in the mid-1990s could not fully account for the dramatic, non-linear increase in reflectance seen at opposition, whereas subsequent versions incorporating coherent backscatter successfully replicate this phenomenon.

In this chapter, we present an overview of fundamental photometric properties of icy surfaces throughout the Solar System and investigate the extent to which these properties reflect the evolution of the bodies on which they reside. We review photometric models and their parameters and discuss the physical interpretability of those parameters. At present, no photometric model accurately retrieves physical characteristics of icy surfaces that can be reproduced in a laboratory setting. Parameters such as albedo, roughness, and porosity are intimately linked, and their degeneracy has not been broken. Owing to this current limitation, we do not provide any model-dependent photometric parameters previously derived for icy surfaces. Instead, we focus on those fundamental photometric properties, primarily albedo and the near-opposition phase function, which are independent of any interpretation from the application of a photometric model. Finally, we offer suggestions for future work, both observational and laboratory measurements, which will enhance the scientific return from continued photometric studies of icy bodies in the Solar System.

2.2 Fundamental Photometric Properties

Several important photometric quantities characterize the energy balance on a planetary surface. These include the geometric albedo, the spherical albedo, the bolometric Bond albedo, and the phase integral. For icy bodies, these are especially important because they direct the nature of volatile transport.

The geometric albedo p_λ at wavelength λ is the ratio of the scattered, integrated flux at opposition to that of a perfectly diffuse, flat disk of the same apparent size.

Geometric albedos are sometimes misleadingly cited as percentages; however, since p_λ is simply a ratio, there is no upper limit on its value. Furthermore, geometric albedos greater than unity invoke no violations of conservation of energy. The bolometric Bond albedo, however, is the total scattered energy from a body divided by the incident energy. It is thus a measure of the total energy balance, and unless a planetary body is self-luminous, the bolometric Bond albedo cannot exceed unity. Recently, the *Cassini* spacecraft measured the bolometric Bond albedos of several saturnian satellites (Howett et al. 2010; Pitman et al. 2010).

The phase integral is given by $q_\lambda = 2\int_0^\pi \Phi_\lambda(\alpha)$ where α is the solar phase angle and $\Phi_\lambda(\alpha)$ is the disk-integrated reflectance normalized to unity at $\alpha = 0°$. The solar phase angle is the angle subtended at the detector between a planetary body and the Sun. The spherical albedo A_λ is the product of the geometric albedo and phase integral and is sometimes referred to as the Bond albedo.

Table 2.1 lists the geometric albedo, phase integral, and spherical albedo measured in the broadband V filter (centered at 0.55 μm) for several giant planet satellites and rings, jovian Trojan asteroids, TNOs (segregated according to the classification of Gladman et al. 2008), comet nuclei, and the icy main-belt asteroid 24 Themis. Although photometric measurements exist for many more objects than those listed here, we only include those of known diameters for which at least rudimentary phase curves are available in the V band. Because the geometric albedo relates the reflectance to that of a diffuse disk of the same apparent size, the diameter of the object must be known in order to determine its geometric albedo. Stansberry et al. (2008) and Müller et al. (2010) applied the standard thermal model (Lebofsky and Spencer 1989) to mid-infrared (24–160 μm) observations acquired by the *Spitzer Space Telescope* and *Herschel Space Observatory*, respectively, to determine the size and albedo of several TNOs.

2.2.1 Geometric Albedo and Phase Function

At opposition, the observer is directly aligned between the planetary body and the Sun, and the solar phase angle reaches a minimum. Since the Sun is not a point source and has a finite angular size, no planetary body can be observed at precisely $\alpha = 0°$. Near opposition, many different phase angles are observed simultaneously due to the angular extent of the solar disk, and the resulting reflectance is a weighted combination of the reflectances measured at all phase angles across the Sun. Therefore, the angular radius of the solar disk seen from a planetary body defines the minimum phase angle at which the object can be observed. Owing to solar limb darkening, phase angles smaller than the angular solar radius are observable during node crossings. Therefore, although the angular size of half the solar disk at 9.5 AU is 0.028°, the minimum phase angle at which a saturnian satellite can be observed is $\sim 0.010°$. The large heliocentric distances of TNOs make it possible to observe them at even smaller phase angles and probe regions of the solar phase curve (reflectance vs. solar phase angle) inaccessible to giant planet satellites. The angular size of the solar radius at 50 AU is 0.005° and solar limb darkening permits access to

Table 2.1 Fundamental photometric quantities for icy surfaces in the solar system[a]

Object	Geometric albedo p_V	Phase integral q_V	Spherical albedo A_V	S_V (mag)	Minimum α observed (angular solar radius) (°)	Refs[b]
Jovian satellites					(0.0512)	
Europa	1.02	0.69	0.70	0.24	*0.02*[c]	*1*
Ganymede (L)	0.61	0.69	0.42	0.277	0.4	*2*
Ganymede (T)	0.42	0.64	0.27	0.027	1.4	*2*
Callisto (L)	0.22	0.59	0.13	0.115	0.4	*2*
Callisto (T)	0.25	0.52	0.13	0.113	0.6	*2*
Jovian trojans	0.03–0.06			0.06	0.051–0.1 (0.052)	*3,4*
Achilles	0.038–0.051			0.045	0.08 (0.052)	*3,5*
Saturnian rings						
A Ring	0.52			0.404	*0.01*	*6*
B Ring	0.79			0.363	*0.01*	*6*
C Ring	0.083			0.498	*0.01*	*6*
Saturnian satellites					(0.0285)	
Janus	0.71			0.352[U]	*0.01*	*7*
Epimetheus	0.73			0.229[U]	*0.01*	*7*
Mimas	0.962	0.62	0.60	0.331	*0.01*	*7*
Enceladus	1.375	0.68	0.93	0.271	*0.01*	*7*
Tethys	1.233	0.52	0.64	0.321	*0.01*	*7*
Calypso	1.34				*0.01*	*7*
Dione	0.998	0.70	0.70	0.302	*0.01*	*7*
Helene	1.67				*0.01*	*7*
Rhea	0.949	0.63	0.60	0.374	*0.01*	*7*
Iapetus	0.30				*0.01*	*7*
Phoebe	0.086	0.32	0.03	0.243	*0.01*	*8*
Uranian rings	0.050	0.36	0.018	0.091	0.034 (0.014)	*9*
Uranian satellites					(0.014)	
Portia group[d]	0.080	0.33	0.026	0.225	0.034	*9*
Puck	0.104	0.34	0.035	0.219	0.034	*9*
Miranda	0.464	0.44	0.200	0.410	0.034	*9*
Ariel	0.533	0.43	0.230	0.441	0.034	*9*
Umbriel	0.258	0.39	0.100	0.321	0.034	*9*
Titania	0.350	0.46	0.170	0.357	0.034	*9*
Oberon	0.309	0.44	0.140	0.359	0.034	*9*
Neptunian satellites					(0.009)	
Triton	0.77	1.16	0.89	0.21	*0.004*	*10, 11*
Nereid	0.26			0.203	*0.005*	*12*
Dwarf planets						
Pluto	0.61			0.0355	0.361 (0.007)	*13*
Charon	0.431			0.265	0.361 (0.007)	*13*
Eris	0.96			0.105	0.16 (0.003)	*14, 15*
Haumea	0.84			0.11	0.51 (0.005)	*16*
Makemake	0.8			0.054	0.69 (0.005)	*17, 15*
Classical KBOs						
Quaoar	0.172			0.159	0.17 (0.006)	*18, 15*
Varuna	0.16			0.278	0.06 (0.006)	*17, 15*
Sila-Nunam	0.06–0.14			0.98[R]	*0.006* (0.006)	*19, 20*

(continued)

Table 2.1 (continued)

Object	Geometric albedo p_V	Phase integral q_V	Spherical albedo A_V	S_V (mag)	Minimum α observed (angular solar radius) (°)	Refs[b]
1999 DE_9	0.0685			0.128	0.17 (0.007)	*17, 15*
2002 KX_{14}	0.60			0.159	0.09 (0.007)	*18, 15*
2002 AW_{197}	0.1177			0.128	0.17 (0.006)	*17, 15*
2002 UX_{25}	0.115			0.158	0.02 (0.006)	*17, 15*
Scattered Disk TNOs						
1999 TD_{10}	0.044			0.15	0.26 (0.013)	*17, 15*
Detached TNOs						
Sedna	0.16			0.114	0.27 (0.003)	*17, 15*
Centaurs						
Chiron	0.0757			0.1	0.64 (0.016)	*17, 21*
Chariklo	0.0573			0.05	4.0 (0.019)	*17, 22*
Bienor	0.0344			0.095	0.33 (0.014)	*17, 15*
2002 PN_{34}	0.0425			0.043	0.33 (0.020)	*17, 15*
Asbolus	0.0546			0.05	1.97 (0.018)	*17, 15*
Thereus	0.0428			0.072	0.22 (0.022)	*17, 15*
Hylonome	0.062			0.206^R	0.09 (0.012)	*23, 24*
Echeclus	0.0383			0.22	0.11 (0.034)	*17, 25*
Typhon	0.051			0.126	0.19 (0.014)	*17, 15*
Plutinos						
Ixion	0.12			0.133	0.03 (0.006)	*17, 15*
Huya	0.0504			0.155	0.28 (0.009)	*17, 15*
1999 TC_{36}	0.0718			0.131	0.28 (0.009)	*17, 15*
2000 GN_{171}	0.0568			0.143	0.02 (0.009)	*17, 15*
Orcus	0.1972			0.114	0.39 (0.006)	*17, 15*
Comets						
19P/Borrelly	0.072	0.26	0.019	0.043	1.9 (0.046)	*26*
2P/Encke	0.047			0.05	4.01 (0.134)	*27*
9P/Tempel 1	0.056	0.23	0.013	0.046	3.24 (0.134)	*28*
81P/Wild 2	0.059	0.16	0.0093	0.0513	13.1 (0.089)	*29*
Main Belt asteroids						
24 Themis	0.074			0.1	0.34 (0.084)	*30,31*

[a]All observations at *V*-band, 0.55 μm, except those noted with[U] which are *U*-band at 0.34 μm and [R]which are *R*-band at 0.65 μm. Unless noted by L (leading hemisphere) and T (trailing hemisphere), all parameters are global averages from rotationally corrected phase curves. Some TNO phase curves have not been corrected for light curve variations

[b]References: *1* Helfenstein and Shkuratov (2011), in preparation, *2* Domingue and Verbiscer (1997), *3* Fernandez et al. (2003), *4* Schaefer et al. (2010), *5* Shevchenko et al. (2009), *6* French et al. (2007), *7* Verbiscer et al. (2007), *8* Miller et al. (2011), *9* Karkoschka (2001), *10* Buratti et al. (2011), *11* Hillier et al. (1990), *12* Schaefer et al. (2008), *13* Buie et al. (2010), *14* Sicardy et al. (2011), *15* Rabinowitz et al. (2007), *16* Rabinowitz et al. (2006), *17* Stansberry et al. (2008), *18* Brucker et al. (2009), *19* Müller et al. (2010), *20* Rabinowitz et al. (2009), *21* Lazzaro et al. (1997), *22* Davies et al. (1998), *23* Luu and Jewitt (1996), *24* Bauer et al. (2003), *25* Rousselot et al. (2005), *26* Li et al. (2007a), *27* Boehnhardt et al. (2008), *28* Li et al. (2007b), *29* Li et al. (2009), *30* Chernova et al. (1994), *31* Harris et al. (1989)

[c]Italicized phase angles are smaller than the solar radius seen from the icy surface

[d]Includes the seven innermost satellites of Uranus: Bianca, Cressida, Desdemona, Juliet, Portia, Rosalind, and Belinda

phase angles as small as $\sim 0.002^\circ$. These configurations describe *true* opposition when the Earth (or spacecraft) actually transits the solar disk as seen from the object.

Traditionally, geometric albedos are determined by extrapolating solar phase curves to opposition, or zero phase. If solar phase curves were simply linear functions, this technique would yield accurate results; however, as phase angles approach zero, phase curves of most particulate surfaces exhibit a dramatic, non-linear increase in reflectance. (We discuss this opposition effect, or surge, in detail in Sect. 2.3.1.4) The best estimates of p_V are therefore achieved when the surface is observed at phase angles close to zero, limited by the angular size of the solar radius seen from the object. Table 2.1 also lists the minimum phase angle at which each icy body has been observed as well as the angular size of the solar radius seen from each. The likelihood that an estimated p_V is close to the actual p_V can be gauged from the minimum observed phase angle. The minimum phase angles at which comet nuclei have been observed, for instance, are rather large (1.9–13.1°); therefore, their geometric albedos are likely underestimates. On the other hand, *Hubble Space Telescope* observations of the uranian satellites and rings (Karkoschka 2001) were obtained at a phase angle ($\alpha = 0.034^\circ$) so close to zero that their measured geometric albedos will probably not significantly exceed these extrapolated values. A growing number of icy bodies have been observed at or near node crossings, enabling *measurement* rather than estimation of their geometric albedo. These include most saturnian satellites (Verbiscer et al. 2007), Nereid (Schaefer et al. 2008), Triton (Buratti et al. 2011), the classical TNO Sila-Nunam (provisionally designated 1997 CS_{29}) (Rabinowitz et al. 2009; Verbiscer et al. 2010), and a few objects for which we do not have geometric albedos, e.g. Tithonus (a Jupiter Trojan (Schaefer et al. 2010)).

A phase function parameter S_V (fifth column in Table 2.1) is simply the difference in reflectance (in magnitudes) observed at solar phase angle 1° and the best estimate (in most cases) of the reflectance at the minimum phase angle at which the body can be observed. Traditionally, the phase coefficient β measures the slope of the phase curve (in magnitudes/degree) over a specified range of phase angles. The phase function parameter S_V may not necessarily be the slope of the phase curve between $\alpha = 0^\circ$ and $\alpha = 1^\circ$, since some phase curves become non-linear at phase angles less than 1°. The parameter S_V simply provides a quantitative measure of the amount by which the reflectance of these icy surfaces increases as they reach opposition. As we discuss in detail below, comparisons between S_V and p_V among icy surfaces throughout the Solar System suggest correlations between their fundamental photometric properties and weathering and thermal histories.

2.2.2 Discussion

At visible wavelengths, geometric albedos of icy bodies throughout the Solar System appear to span a broad range, from 0.03 to 1.4. Closer inspection reveals, however, that only the major satellites closest to the giant planets and the dwarf planets have $p_V > 0.2$ and the surfaces of most other icy bodies are dark ($p_V < 0.2$). The major satellites of the outer Solar System orbit within giant planet magnetospheres in

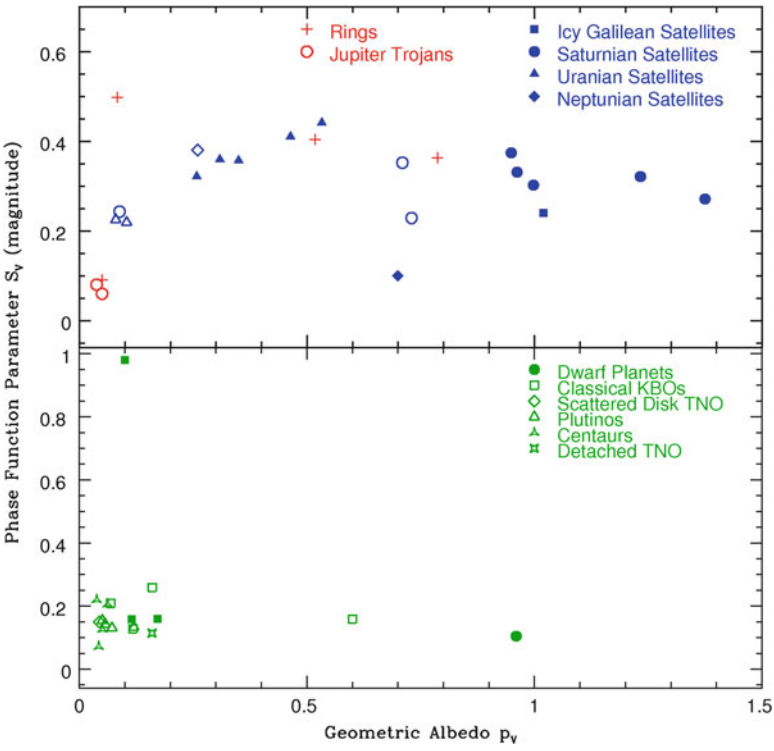

Fig. 2.1 Geometric albedo p_V and a phase function parameter S_V for icy surfaces in Table 2.1 which have been observed at phase angles smaller than 0.3°. S_V is the slope of the phase *curve* between $\alpha = 1°$ and $\alpha = 0°$, measured in magnitudes. In most cases the reflectance at $\alpha = 0^o$ is derived from extrapolating the phase curve to opposition. For the saturnian satellites, Nereid, Triton, and Sila-Nunam the reflectance at true opposition was measured rather than extrapolated from solar phase curves. For the objects in the *upper box*, *solid symbols* denote objects larger than 300 km in diameter; for the TNOs in the *lower box*, solid symbols represent binary systems

regions populated by dust and charged particles. These environments alter physical surface properties through processes such as sputtering and desorption (e.g. Paranicas et al. 2009), micrometeoroid impacts (e.g. Verbiscer et al. 2007), and sublimation (cf. Spencer 1987). As a result, these satellite surfaces exhibit a wide variety of albedos, colors, and phase functions on both global and small scales while most TNOs, irregular satellites and Trojans, have more uniform colors, or at least groupings of colors, albedos, and phase functions.

To investigate the correlation of albedo and phase function with various types of icy surfaces, Fig. 2.1 shows both quantities for those objects which have been observed at phase angles smaller than 0.3°. Icy surfaces which have not been observed at $\alpha < 0.3°$ are excluded because their geometric albedos and phase functions are likely underestimates and their placement on Fig. 2.1 would be misleading. Several groupings appear, most notably the major saturnian and uranian satellites. The satellites residing within Saturn's tenuous E ring all have

geometric albedos at or above unity, and Mimas, Enceladus, Tethys, and Dione have $S_V > 0.25$ mag due to continuous bombardment by E ring particles (Verbiscer et al. 2007). Janus and Epimetheus also orbit Saturn within their own dusty ring which accounts for their high geometric albedos and steep phase functions. Although Phoebe also orbits Saturn within its own dusty ring (Verbiscer et al. 2009), the relatively lower impact velocities between Saturn's darkest satellite and ring particles produce a shallower phase function than that seen on moons closer to the planet. While there is no apparent correlation between size and phase function S_V, icy bodies larger than 300 km in diameter (solid symbols at the top of Fig. 2.1) are brighter ($p_V > 0.25$) than smaller objects.

The exceptionally high geometric albedo of Enceladus is consistent with the fact that it is geologically active (Spencer et al. 2006). Triton also has a high geometric albedo (Buratti et al. 2011) and is geologically active (Soderblom et al. 1990). Even with substantial magnetospheric bombardment and darkening, Europa's high albedo indicates that its surface has far more fresh exposed water ice and less surface contaminants than Ganymede and Callisto. Full-disk observations of the icy Galilean satellites do not exist at phase angles smaller than 0.2°; therefore, their geometric albedos are likely not accurately extrapolated from their phase curves. The geometric albedo of Europa is derived from a "hybrid" phase curve comprised of disk-resolved *Galileo* spacecraft observations and full-disk reflectances (discussed in detail in Sect. 2.3.1.5). The geometric albedo of the classical Kuiper belt object (KBO) 2002 KX_{14} is unusually high ($p_V = 0.6$); however, the uncertainties in this measurement are also large +0.36 −0.23 (Brucker et al. 2009). The only other bodies with $p_V > 0.5$ are dwarf planets Pluto, Eris, Makemake, and Haumea, yet it is not currently known if any of these bodies is geologically active. Only Eris has been observed at $\alpha < 0.3°$, so it's possible that the other dwarf planets have even higher geometric albedos and steeper phase functions. Most distant, irregular satellites, including Phoebe, are dark. When considered along with their retrograde orbits, the low albedo of these objects suggests that they were captured and did not originate with their parent planet but elsewhere in the Solar System.

The Solar System's most reflective satellites, Enceladus and Tethys, interestingly, do not have the steepest phase functions. Although the major uranian satellites (Miranda, Ariel, Umbriel, Titania, and Oberon) are substantially darker than their saturnian counterparts, they exhibit comparable phase functions S_V. Miranda and Ariel have the steepest phase functions of any icy satellites, yet the exact mechanism by which their phase functions are enhanced is not currently known. Only particles in Saturn's C-ring demonstrate a more dramatic increase in reflectance as the phase angle decreases from 1°. The phase functions of the saturnian rings are anti-correlated with albedo. Section 2.3.1.4 discusses the relationship between albedo and the coherent backscatter opposition effect.

Aside from Saturn's C ring, the darkest objects in the Solar System have relatively shallow phase functions $S_V < 0.25$. These include comet nuclei, Centaurs, jovian Trojans and particles comprising the uranian rings. The Centaurs and jovian Trojans are the darkest objects ($0.03 < p_V < 0.08$). The surfaces of Plutinos, objects in a 3:2 mean motion resonance with Neptune, and comet nuclei

are similarly dark. Among the TNOs, a handful of classical KBOs (Varuna, Sila-Nunam, 2002 KX_{14}, and 2002 UX_{25}), two Centaurs (Hylonome and Echeclus), and two Plutinos (Ixion and 2000 GN_{171}) have been observed at phase angles smaller than $\alpha \approx 0.1^{\circ}$. Interestingly, some jovian Trojans have been observed at phase angles close to the angular solar radius at their heliocentric distance, yet they have very small S_V. Other objects with comparably small S_V have not been observed at phase angles near the minimum as the jovian Trojans have, thus, their phase functions are likely underestimated.

The rest of the objects in these groups will likely move slightly upward and to the right in Fig. 2.1 as they are observed at smaller phase angles. The classical KBOs in dynamically "cold" orbits with low inclinations and low eccentricities have generally higher geometric albedos than Sedna, a "detached" object (having no influence from Neptune or any other giant planet), and 1999 TD_{10}, a TNO from the scattered disk. However, more detached TNOs and objects from the scattered disk need to be observed at small phase angles to reach statistically valid conclusions. Except for the dwarf planets, all TNOs exhibit roughly similar S_V. Sila-Nunam, the classical binary KBO which has been observed at the smallest (but not minimum) phase angle, also has the steepest phase function. Rabinowitz et al. (2009) and Verbiscer et al. (2010) suggest that ejecta exchange between binary or multiple components of TNOs (Stern 2009) can produce the surface microtextures capable of enhancing the reflectance at opposition. Solid symbols in the lower portion of Fig. 2.1 represent binary or multiple TNO systems. Excluding Sila-Nunam, however, there does not currently appear to be a strong correlation between TNOs with multiple components and phase function.

2.3 Photometric Models and Their Parameters

Photometric models have been widely applied to icy bodies in the Solar System for many years. They all strive to relate viewing geometry to the radiance factor R_λ, where $R_\lambda = I_\lambda / F_\lambda$. I_λ is the specific intensity of light at wavelength λ scattered from a surface and πF_λ is the plane-parallel specific incident solar flux. The radiance factor itself is dimensionless since I_λ and πF_λ both have units W/m^2/sr. Typically, radiance factors range from 0 to 1. Most often, broadband photometry is obtained from spacecraft imaging cameras and telescopes, and the radiance and flux quantities are then integrated over the specific optical filter bandpass being used for the observation.

Empirical equations, such as that of Lambert (1760), Minnaert (1941) and Kaasalainen (2003), relate the reflectance from a particulate surface to viewing geometry in a simple manner as functions of the incidence, emission and solar phase angles. The incidence angle i is the angle between the surface normal and the incident radiation, while the emission angle e is the angle between the surface normal and emergent ray. The solar phase angle α is the angle between the incident and emergent ray, measured from the scattering surface. (See Verbiscer and Helfenstein (1998) for a detailed review of empirical models.) Analytical models,

such as that of Hapke (1981, 1984, 1986, 2002, 2008), Goguen (1981), Lumme and Bowell (1981, 1985), and Shkuratov et al. (1999) approximate the solution for radiative transfer from a rough, particulate surface.

An analytical photometric model can be best considered as an assemblage of mathematical components, each of which describes a functional dependence of directional light scattering on a different parameterized quasi-physical property, or a group of related properties that act in concert. The main functional components of typical models rely on (1) a component to describe albedo and directional singly scattered light by an average regolith grain, (2) a component to describe how photons are multiply scattered among and from an aggregate volume of average grains, (3) a parameterized component to describe the effects of macroscopic surface texture on reflected light, and (4) component functions to describe the opposition effect – a conspicuous non-linear surge in brightness with decreasing phase angle that is observed at small phase angles on particulate covered bodies. So complex are these interactions that even the best available analytical models remain incomplete and inadequately verified. They have continued to evolve over a span of at least three decades as laboratory testing and refinement of theory identify new deficiencies and new corrections, respectively. One of the most difficult aspects of summarizing the results of photometric analyses from a wide variety of icy surfaces is that over the past few decades, different versions of the models have been used to analyze different icy body data sets. Since the last review of the photometric properties of solar system ices (Verbiscer and Helfenstein 1998), there have been a number of advances in the theories used to interpret photometric data and observations as well as advances in the analysis and realization of the limits of currently available models (Shepard and Helfenstein 2007). Among the analytical models, the Hapke (1981, 1984, 1986, 2002, 2008) model and the Shkuratov et al. (1999) model have seen the widest application to both photometric and spectroscopic data. We discuss below recent modifications to the Hapke model and a model based on that of Shkuratov et al., presenting their parameters and the physical interpretability of those parameters.

2.3.1 The Hapke Model

Among the analytical models, Hapke's (1981, 1984, 1986, 2002, 2008) equation has seen the widest application to icy surfaces. In general, the Hapke function yields useful, high-fidelity modeling of the photometric behavior of planetary regoliths. It is well-suited to image processing tasks such as correcting for systematic photometric shading gradients across the disk in spacecraft images so that they can be used as panels in global albedo maps, or for estimating radiometric Bond albedos. However, despite numerous revisions and refinements to overcome deficiencies and improve its physical realism, the Hapke model has yet to be fully validated as a tool for retrieving accurate estimates of the physical and geological properties of planetary regoliths. Until accurate soil physical properties can be verifiably retrieved

from fits of Hapke's model to well-characterized laboratory samples, the validity of many published studies that adopt this approach remains in doubt. Further, few published planetary photometric analyses make use of the most recent version (Hapke 2008) that corrects a fundamental flaw in earlier treatments of the effects of regolith porosity on reflectance. Consequently, nearly all published applications of Hapke's model to planetary objects are obsolete and mutually inconsistent.

Only limited success has been realized in attempts to validate Hapke theory by comparing the known characteristics of laboratory samples to those predicted by fits of the model parameters to photometric observations of the samples. Gunderson et al. (2006) performed fits of Hapke's (2002) model to a sample of JSC-1 lunar soil stimulant. While they obtained excellent fits to fixed incidence angle, variable emission angle data sets, the models extrapolated poorly to fixed, near-zero phase angle data at varying incidence angles, and no solutions provided simultaneous, high quality fits to the two types of data sets. Strong correlations were found between single-scattering albedo and the particle phase function parameters and, to a lesser extent, the small-scale mean surface roughness. Shepard and Helfenstein (2007) performed fits of Hapke's (2002) model to spectrophotometric measurements covering a wide range of photometric geometries of soil analogs for 29 separate particulate samples (both natural and artificial) and compared their results to the known composition, compaction state, grain-size distribution and particle structure of the samples. They found no compelling evidence that individual photometric parameters could be uniquely interpreted to reveal the physical state of the samples, either in an absolute or relative sense. Instead, combinations of physical properties such as particle single-scattering albedo, roughness, and porosity were convolved within each retrieved photometric parameter. Shkuratov et al. (2007) tested the validity of Hapke (2002) model inversions for natural particulate sample surfaces when the directional scattering behavior (that is, the particle phase functions) of isolated natural soil grains are independently known from polar nephelometer measurements. Like Shepard and Helfenstein (2007), they found that retrieved values of particle single-scattering albedo depended on the compaction state of the soil samples, contrary to model predictions. They also found a wavelength-dependence for Hapke model parameters that, in theory, should not depend on wavelength.

In the most recent and promising attempt to validate Hapke's (2008) model, Helfenstein and Shepard (2011) updated Hapke's (1986) model of the shadow-hiding opposition surge to be consistent with the 2008 correction for porosity. In a preliminary test, the refined model was fit separately to three samples from Shepard and Helfenstein's (2007) suite of laboratory photometric measurements representing respectively, a low-albedo, a medium albedo, and a very high-albedo surface. The test suggests that the revised Hapke model significantly improves the fidelity of model parameters retrieved for low- to moderate-albedo materials. However, as predicted by Hapke's (2008) theory, the porosity correction has little effect on high-albedo surfaces for which no improvements were observed in the test. Much more thorough testing is needed, but for application to icy satellite surfaces, the preliminary tests imply that reliable results can be obtained only at spectral wavelengths where ice particles are dark, for example, in the ultraviolet range.

2.3.1.1 Single Scattering by Average Regolith Grains

Light that is scattered once by an average regolith grain is generally described by the product $\omega_o P(\alpha)$ where ω_o is the average particle single scattering albedo and $P(\alpha)$ is known as the average particle single scattering phase function. The single scattering albedo is the ratio of a particle's scattering efficiency to its extinction efficiency, or the probability that a photon will be scattered rather than absorbed. Hapke's models prior to 2008 do not properly treat how the effective scattering cross sections of regolith grains in mutual contact change with changing packing density or porosity. As a result, estimates of ω_o retrieved from fits of the earlier models to photometric data can be significantly in error.

As noted above, the single particle phase function describes the directional scattering behavior of average regolith grains. Although Hapke (1981) initially proposed using a two-parameter Legendre polynomial representation, typically the empirical one-term Henyey-Greenstein (1941) phase function (1THG) is used:

$$P(\alpha) = \left(1 - g^2\right)/(1 + 2\,g\cos(\,\alpha) + g^2)^{3/2}$$

The asymmetry parameter g is the average cosine of the scattering angle Θ, and $\Theta = \pi - \alpha$. By convention, g ranges from -1 to $+1$, with negative values representing backscattering and positive values representing forward scattering behavior. Particles which scatter isotropically have $g = 0$. To data sets which span nearly the full range of phase angles, a double Henyey-Greenstein function is sometimes used to describe anisotropic particle scattering. This can be a three-term Henyey-Greenstein function (3THG) which is a linear combination of two 1THG's (cf. Kattawar 1975):

$$P(\alpha) = (1-f)\frac{(1-{g_1}^2)}{(1+2g_1\cos(\alpha)+{g_1}^2)^{3/2}} + (f)\frac{(1-{g_2}^2)}{(1+2g_2\cos(\alpha)+{g_2}^2)^{3/2}} \quad (2.1)$$

where g_1 and g_2 are separate asymmetry parameters that, most often, describe backward and forward scattering lobes, respectively, of different angular widths, and the partition parameter f controls the relative amplitude of each contribution. In two-term simplifications (2THG) of the Henyey-Greenstein models, the forward and backscattering components have the same angular widths but different amplitudes. The most often used representation is that from McGuire and Hapke (1995)[1]:

$$P(\alpha) = \frac{(1+c)}{2}\frac{(1-b^2)}{(1-2b\cos(\alpha)+b^2)^{3/2}} + \frac{(1-c)}{2}\frac{(1-b^2)}{(1+2b\cos(\alpha)+b^2)^{3/2}} \quad (2.2)$$

In relation to the 3THG parameters from Eq. 2.1, $g_1 = -g_2 = -b$ and $f = (1 - c)/2$. Most icy bodies in the Solar System are dominantly backscattering

[1] Domingue et al. (1991) and Souchon et al. (2011) adopted a slightly different version of the 2THG in which coefficients c and $(1 - c)$, respectively, replace $(1 + c)/2$ and $(1 - c)/2$ in Eq. 2.2.

(Verbiscer et al. 1990); although, those to which a double Henyey-Greenstein phase function has been applied also exhibit a forward scattering component (Hillier et al. 1990; Domingue and Verbiscer 1997; Buratti et al. 2008).

Physical interpretability: For macroscopic regolith grains in mutual contact (as in a regolith), the directional scattering of light is sensitive to the shape, microscopic texture, internal mechanical structure, and optical constants of the materials composing the particles. McGuire and Hapke (1995) attempted to map out the relationship between parameters of their 2THG particle phase function and the well-characterized structural properties of analog regolith particles in the laboratory. In theory, their results provide a framework for interpreting the physical structure of average regolith grains from fits of the 2THG retrieved from photometric phase curves of planetary surfaces. However, in their laboratory test, Shepard and Helfenstein's (2007) retrievals of the 2THG parameters only crudely reflected the characteristics of grains making up the samples. Souchon et al. (2011), on the other hand, tested Hapke's (1993) model and found good qualitative agreement between the observed microstructure of natural soil grains and the physical interpretation of retrieved particle phase function model parameters when the range of photometric geometries of the samples were optimized to exclude the opposition effect and observations at large incidence and emission angles.

2.3.1.2 Multiple Scattering

Many of the changes in Hapke's model as it has been applied to icy satellites have come through refinement of the function to describe the contribution of multiply-scattered photons between grains in the regolith. Hapke's (1981, 1984, 1986) model approximated multiple scattering with an analytical simplification of Chandrasekhar's (1960) H-functions for isotropically scattering grains. This approximation was considered adequate for relatively low to moderate albedo bodies for which the contribution of multiply scattered light was small compared to the emitted singly scattered signal. It was also applied in early Voyager-spacecraft based studies of icy satellites (Helfenstein 1986; Verbiscer and Veverka 1989; Domingue et al. 1991). During the 1990s some icy satellite studies improved the Hapke model by substituting the exact calculation for anisotropic scatterers (Verbiscer 1991; Verbiscer and Veverka 1992, 1994). As more complete phase coverage of icy satellites became available through *Galileo* and *Cassini* spacecraft data, Hapke (2002) anticipated the need for a rigorous treatment of multiple scattering for strongly anisotropic grains and introduced such an improvement as well as more accurate analytical approximations for multiple scattering by isotropic scatterers.

2.3.1.3 Macroscopic Roughness

Hapke's (1984) macroscopic roughness parameter θ encompasses topographic facets ranging in size from aggregates of particles to mountains, craters, and ridges, up to the spatial resolution limit of the detector on the surface (Helfenstein 1988;

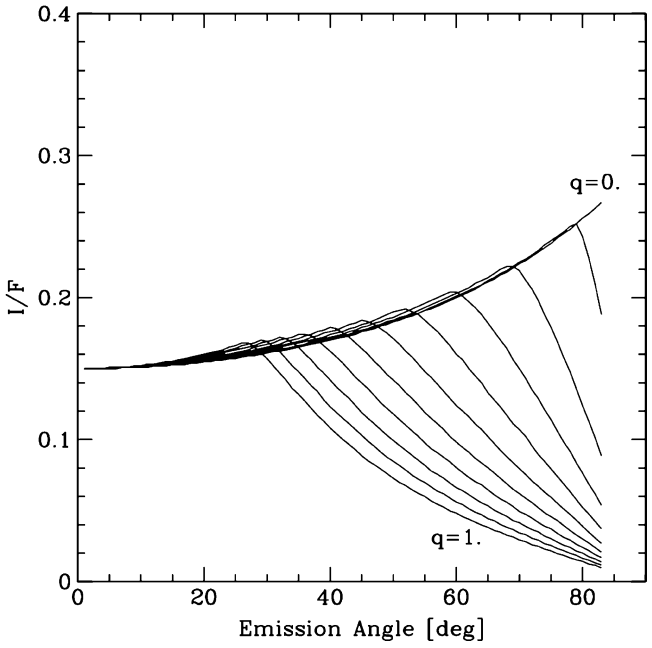

Fig. 2.2 Scans of the radiance factor (I/F) along the photometric equator for a solar phase angle of 24° and for a variety of crater depth-to-radius ratios (q) ranging from 0 (*smooth*) to 1 (*rough*). An inflection point occurs in the scan that is characteristic of the roughness: fitting observations to disk-resolved observations from spacecraft can effectively derive surface roughness

Shepard and Campbell 1998; Helfenstein and Shepard 1999). These topographic features alter the specific intensity of an icy surface by changing the local incidence and emission angles from that of a smooth locally flat surface, by removing radiation from the scene from cast shadows, and through occultation of some surface facets by others. In addition to the analytical mean slope model used by Hapke, numerical models such as the crater roughness model (Buratti and Veverka 1985) and the S-matrix model (Goguen et al. 2010) describe this effect quantitatively. Figure 2.2 shows an example of how a rough facet alters the reflected intensity at the photometric equator.

Three main problems exist in deriving macroscopic roughness from spacecraft and ground-based observations: (1) the non-uniqueness of the formal fits, (2) the treatment of volumetric multiple scattering, including the absence of a treatment for multiple reflection at macroscopic scales, and (3) the improper treatment of the effects of porosity in formulations prior to Hapke (2008). The difficulty with obtaining a unique determination of roughness can be minimized by obtaining observations over a range of solar phase angles and by fitting models to both disk-integrated and disk-resolved measurements (Helfenstein et al. 1988). In general, the effects of macroscopic roughness are most pronounced at large solar phase angles. However, it is difficult to derive separately the single particle phase function

and roughness, since both quantities show the largest effects at large solar phase angles. In disk-resolved observations, roughness is most strongly manifested by limb-darkening behavior and it is most reliably distinguished on low-albedo surfaces. Unfortunately, in high-albedo surfaces, multiple-scattering of light between regolith grains, introduces additional limb-darkening effects that can complicate the recognition of effects due to roughness. Especially for very high albedo objects, like Enceladus and Europa, one might expect that different roughness estimates could be obtained depending on which model of volumetric multiple scattering was assumed.

Physical Interpretability: Two critical obstacles to the meaningful interpretation of photometric roughness are necessarily limited by the extent to which idealized shapes conform to actual geological features and the tendency of multiply-reflected light to mute the detectible roughness selectively at different size scales depending on the albedo of the surface. No model fully replicates the full range of features found on a planetary surface. Roughness models peer into the topography of the surface *below the resolution limit of the camera*. However the smallest-sized features that contribute to detectible photometric roughness effects depend on the size scale at which projected shadows become dark. Recent work shows that for low-albedo objects like the moon, small sub-millimeter scale features dominate (Helfenstein and Shepard 1999). For high-albedo surfaces, the size-scale at which projected shadows become dark is likely significantly larger. One consequence of this albedo selection effect is that high-albedo surfaces have a tendency to exhibit smaller amplitude photometric roughness than low-albedo surfaces. Shepard and Helfenstein (2007) observed this effect in laboratory tests on a variety of soil samples and found a systematic decrease of photometrically derived values of θ with increasing ω_o. A further consequence is that the types of geological structures that dominate photometric roughness likely change with size scale. On low albedo surfaces, these appear to be aggregates of regolith grains; however, on bright icy satellites, they may be tiny (perhaps centimeter or larger) impact craters.

2.3.1.4 Opposition Effect

Airless planetary bodies typically exhibit a sharp increase in brightness as the phase angle approaches zero. This 'opposition effect' is due to both shadow hiding and a constructive interference phenomenon known as coherent backscatter. The disappearance of mutual shadows cast by particles comprising the regolith (Irvine 1966; Hapke 1986) is most pronounced at phase angles less than 20° (cf. Helfenstein et al. 1988) and is related to the size distribution of regolith grains, their transparency, the porosity of the surface, and the rate at which porosity changes with depth. At the smallest phase angles ($\alpha < 2^{o}$), the coherent backscatter opposition effect (CBOE) occurs when photons following identical but reversed paths in the regolith interfere constructively in the backscattering direction to increase the brightness by up to a factor of two (Shkuratov 1988; Muinonen 1990; Hapke 1990; Mishchenko 1992; Ozrin 1992). While the shadow hiding opposition effect (SHOE) affects only singly

scattered photons, coherent backscatter affects multiply scattered photons, but because multiple scattering can occur within the internal structure of single particles, the Hapke model allows it to amplify both the singly and multiply scattered light (Hapke 2002; Hapke et al. 2009; Helfenstein et al. 1997; Helfenstein and Shepard 2011). If whole regolith grains are the dominant fundamental scatterers of light in a regolith, then CBOE should be important mostly for bright icy surfaces such as Europa and Enceladus. Yet while they are dark in comparison to those objects, the uranian satellites (Karkoschka 2001) and Phoebe (Miller et al. 2011) also have strong opposition surges (Fig. 2.1) attributed to CBOE, and a significant CBOE contribution is seen even in lunar soils (Hapke et al. 1993, 1998; Helfenstein et al. 1997; Shkuratov et al. 1999). In Hapke's 2002 treatment, both CBOE and SHOE are each characterized by an amplitude and an angular width term: $B_{o,sh}$ and h_{sh} for the SHOE respectively, and $B_{o,cb}$ and h_{cb} for CBOE.

Physical Interpretability: The SHOE amplitude, can be interpreted as a measure of regolith grain transparency. The value of $B_{o,sh}$ can range from unity for perfectly opaque grains, to nearly zero for ideally transparent grains. While the SHOE angular width depends on a variety of aspects of grain packing and size distribution, to simplify interpretation in planetary photometric analyses, it is often assumed that over the shallow depth to which optical radiation probes, regolith grains have a uniform size and packing with depth. Under these assumptions, h_{sh} is strictly a function of the porosity: In Hapke (1986), $h_{SH} = -0.375\ \ln(1\text{-}\phi)$, where ϕ is known as the packing-factor and porosity $p = (1\text{-}\phi)$. However, Hapke (2008) noted that this expression is only partly correct. After updating to be consistent with Hapke's porosity correction, Helfenstein and Shepard (2011) determined that

$$h_{SH} = -0.3102\,\phi^{1/3}\ln\left(1 - 1.209\phi^{2/3}\right) \tag{2.3}$$

The angular width parameter of the CBOE, h_{cb}, is primarily sensitive to the mean optical path length of a photon through the regolith. It is thus sensitive to the optical transparency of regolith grain materials, and the arrangement of scatterers both within the regolith and within individual grains in the regolith. Relatively long path lengths are needed to produce a narrow CBOE. The amplitude of the CBOE is sensitive to the intensity of multiple scattering, and to first order should be largest for regoliths (or regolith grains) containing high densities of high-albedo scatterers.

2.3.1.5 Summary of Current Limitations of the Hapke Model

At present, there has been only one published laboratory validation (Helfenstein and Shepard 2011) of Hapke's (2008) correction for the effects of porosity. That study successfully predicted reflectances of well-characterized powders composed of spherical particles with known optical properties given *a priori* knowledge of the packing and size-distribution. However, to date, no blind test that demonstrates successful accurate retrieval of optical and physical sample properties using the Hapke (2008)

Table 2.2 Fits of different Hapke model versions to Europa's (0.55 μm) phase curve[a]

Hapke model	ω_o	h_{sh}	$B_{0,sh}$	h_{cb}	$B_{0,cb}$	g	θ	Residual
1986	0.966	0.00054	1.000	NA	NA	−0.39	16°	0.00119
1993	0.965	0.00053	0.97	NA	NA	−0.39	17°	0.00114
2002	0.952	0.625	1.00	0.0016	0.49	−0.25	18°	0.000993
2008	0.917	0.237	0.49	0.0013	0.47	−0.21	22°	0.000634

[a]Adapted from Helfenstein et al. (in preparation)

correction has been published. Hence, the validity of any physical interpretations of Hapke model fits to icy satellite surfaces to date remains questionable.

It is interesting to compare how different versions of the Hapke model perform on a well-defined phase curve, Table 2.2 and Fig. 2.3 show a preliminary fit of Hapke (2008) to phase curve data for Europa in comparison to fits using earlier versions of the Hapke model to the same data set. Hapke (2008) fits the data better than any of the previous models. All of the fits to the Europa phase curve similarly require a moderately rough surface $(16° \leq \theta \leq 22°)$ composed of relatively high-albedo ice grains $(0.952 \leq \omega_o \leq 0.975)$. However, the fits differ most significantly in terms of the way they resolve the opposition effect and the particle phase function. The 2008 and 2002 models both incorporate the same physical description of CBOE and SHOE. Both resolve the total opposition effect into a narrow angular contribution from CBOE and a relatively broad contribution from SHOE. For the 2008 model, the SHOE angular width is only about 49% as wide and only 38% as intense as for the 2002 model fit. In terms of implied regolith properties, the 2008 model is consistent with a porosity of about 53% among transparent particles, while the 2002 model predicts a more compacted regolith with a porosity of less than 20% among opaque particles. Both of these models work with a moderately backscattering $(-0.25 \leq g \leq -0.27)$ ice grains. Modeling only the SHOE, the Hapke 1981, 1984, and 1986 equations all lack a description of CBOE. Consequently, they manage to fit the Europa data set by forcing the SHOE angular width to fit the narrow (i.e. CBOE) component and by forcing the particle phase function to be strongly backscattering enough to describe the broad SHOE behavior (that was described by SHOE in the 2002 and 2008 models). In other words, the introduction of a separate CBOE model in 2002 provided the SHOE model the freedom to describe a broader component of the opposition effect (cf. Helfenstein et al. 1997; Hapke et al. 1998). In terms of implied regolith properties, these older models predict an unrealistically large porosity (>99%) among opaque regolith grains (cf. Domingue et al. 1991). In summary, among all four model fits, Hapke (2008) is intuitively most realistic because it best describes scattering among bright transparent ice particles (as opposed to implausible opaque grains), and does not require an exotic regolith porosity.

The above demonstration is by no means proof that the Hapke (2008) model is fully correct. As described previously, even with the correction from Hapke (2008), a primary remaining deficiency is the failure of the macroscopic roughness model to account for the effects of multiple reflections from topographic facets. More critical

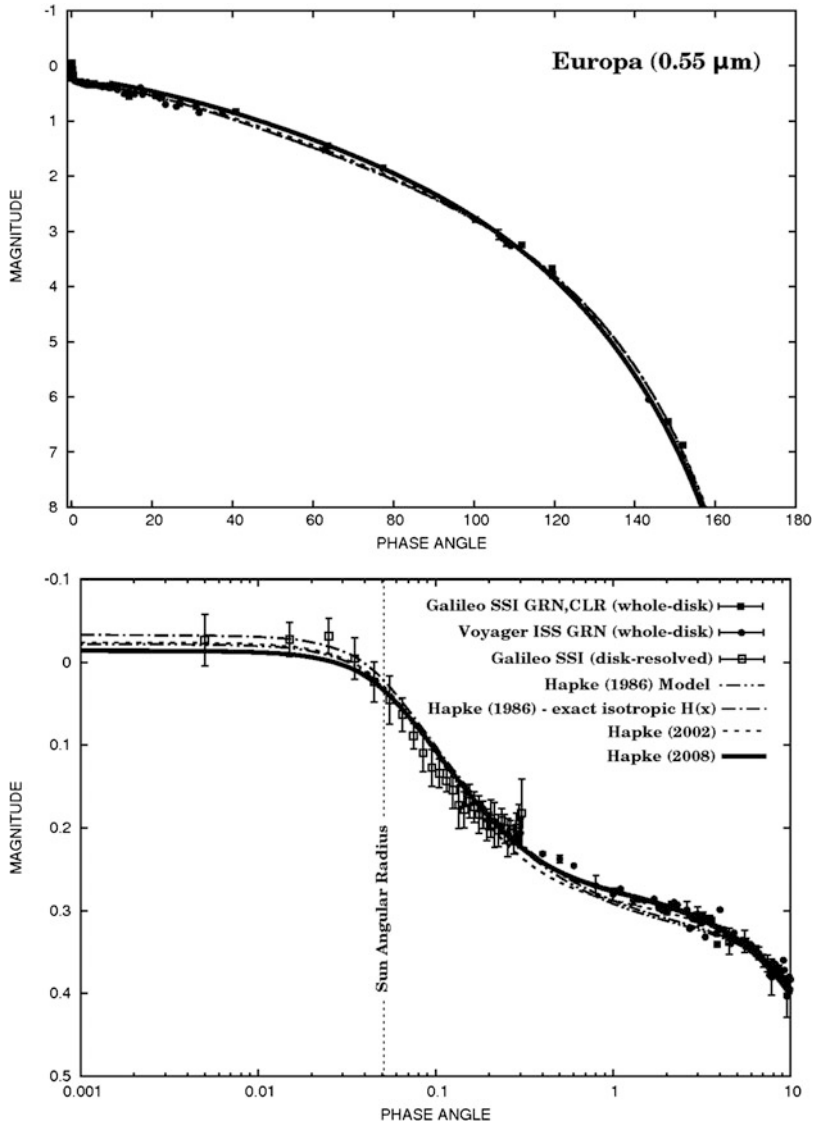

Fig. 2.3 Fits of different versions of Hapke's photometric model (Table 2.2) to Europa's phase curve (Helfenstein et al. in preparation). Observations combine Voyager ISS, Galileo SSI, and Earth based telescopic data. (*top*) Section of phase curve at phase angles less than 10° show details of the opposition effect (note logarithmic scale for phase angles). (*bottom*) Phase curve plotted out to large phase angles. Differences in the phase curve behavior predicted by the different model fits are relatively small

is the potentially fundamental flaw in the Hapke model revealed by laboratory work (Piatek et al. 2004): the Hapke model treats whole regolith grains as the fundamental light-scattering units in planetary soils. Laboratory work by Piatek et al. suggests that the smaller constituents of regolith particles (particle inclusions, crystal

defects, voids, particle surface asperities, and minute dust particles that coat larger grains) may play a more fundamental role in controlling light scattering from typical regolith surfaces.

2.3.2 *Quasi-fractal Photometric Models*

At submillimeter size scales, undisturbed lunar regoliths and presumably regoliths on other airless bodies, exhibit a fractal architecture (cf. Helfenstein and Shepard 1999). It is thus not surprising that photometric models which attempt to treat regolith surfaces realistically as fractal structures have recently been under development (Drossart 1993; Shkuratov et al. 1999; Shkuratov and Helfenstein 2001). The most recent of these sought to develop a realistic model that can account for the simultaneous contributions of SHOE and CBOE in planetary regoliths. By their nature, these models overcome an important limitation of the Hapke model by allowing for the possibility that microscopic dust coating regolith grains, grain imperfections, surface asperities, inclusions may be important fundamental scatterers in regoliths. Shkuratov et al. (1999) introduced a semi-empirical three-parameter photometric model that treats the regolith as a topographically faceted structure with roughness that varies with size scale according to fractal-like statistics (see also Shkuratov et al. 1991). The three model parameters are d, the approximate diameter of an individual scatterer in the regolith, k, a semi-empirical parameter that characterizes the shape of the shadow-hiding opposition surge, and a coherent-backscatter parameter L that represents the diffusion scale-length of photons through the regolith. The model accurately described the lunar opposition effect seen by the *Clementine* spacecraft, as well as the opposition phase curves of asteroids, Phobos, and laboratory analogs. Perhaps the most valuable aspect of this study was its robust model for the CBOE.

2.3.2.1 The Shkuratov-Helfenstein (S-H) Model

Shkuratov and Helfenstein (2001), building on Shkuratov et al. (1999), developed an improved fractal-based light-scattering model that incorporates parts of the Hapke model to replace some of the semi-empirical components. While they adopted the fairly rigorous coherent-backscatter model and the treatment of a fractally faceted surface at large scales from Shkuratov et al. (1991), they more realistically treat regolith grains as fractally-structured aggregates composed of minute "elemental" scatterers. They also incorporate Hapke's (1986) more rigorous treatment of SHOE.

The elemental scatterers in their analytical approximation of a regolith aggregate are assumed to be isotropically scattering grains with a model average single-scattering albedo, ω_o. The relative size and structural complexity of the regolith is characterized by a number of hierarchical generations, η, that must be assembled

to form a regolith with the correct albedo and directional scattering behavior.[2] In this fractal model, the parameter η need not be an integer and can have values less than unity (for example, for icy regolith aggregates that are not perfectly opaque). The model also combines the CBOE and SHOE and describes the way SHOE is manifested on a fractally arranged surface. It employs Hapke's h parameters to describe the angular width of the SHOE and Shkuratov's coherent backscatter parameter L.

Physical Interpretability of S-H Parameters: As stated earlier, the single scattering albedo parameter, ω_o in this model differs from that in the Hapke model in that it characterizes elemental scatterers from which whole regolith grains are composed. In the Hapke model, the single-scattering albedo refers to the albedo of an average whole regolith grain. The equivalent quantity can be computed in the S-H model (see Fig. 2.4 in Shkuratov and Helfenstein 2001) given the other three S-H parameters. The h-parameter has the same meaning and interpretation as it does in Hapke (1986). It measures the angular width of the SHOE and is related to the compaction state of the regolith. The characteristic diffusion length, L, is analogous to the mean optical path length of a photon in the aggregate. In general, larger values of L correspond to narrower CBOE angular widths and greater permeability of regolith materials to scattered photons. Finally, the fractal generation number, η, is a measure of the structural complexity of the regolith. When $\eta \geq 1$, the aggregates are large and structurally complex enough to be opaque. The case where $\eta = 0$ is the limiting condition most like the Hapke model because it represents a regolith in which the elemental scatterers are not aggregated at all, but instead they scatter as whole particles. For bright icy satellites, we often expect the case where $0<h<1$, because this represents an aggregate that is not large and complex enough to be opaque (that is, in this case the regolith grains are partially transparent or translucent).

To date, the S-H model has not been extensively applied to planetary objects for two main reasons. First, until recently, relatively few photometric data sets offered sufficiently detailed phase angle coverage. Meaningful fits of the S-H model require observations at phase angles small enough to detect the CBOE (usually seen at $\alpha < 2^{\circ}$), and the coverage need so extend far enough beyond the SHOE to characterize its shape fully (generally through $\alpha > > 20^{\circ}$). In addition, the model needs further refinement to improve its accuracy for describing photometric behavior at very large phase angles ($\alpha > 120^{\circ}$).

Figure 2.4 and Table 2.2 show trial fits of the S-H model to several objects that cover a range of albedos. These include fits using a revised model that incorporates Hapke's (2008) porosity correction and elemental scatterers that are slightly

[2] In Shkuratov and Helfenstein (2001), the symbol q was used to represent the fractal generation number of the regolith. To avoid confusion with the symbol for phase integral, we adopt the symbol η here.

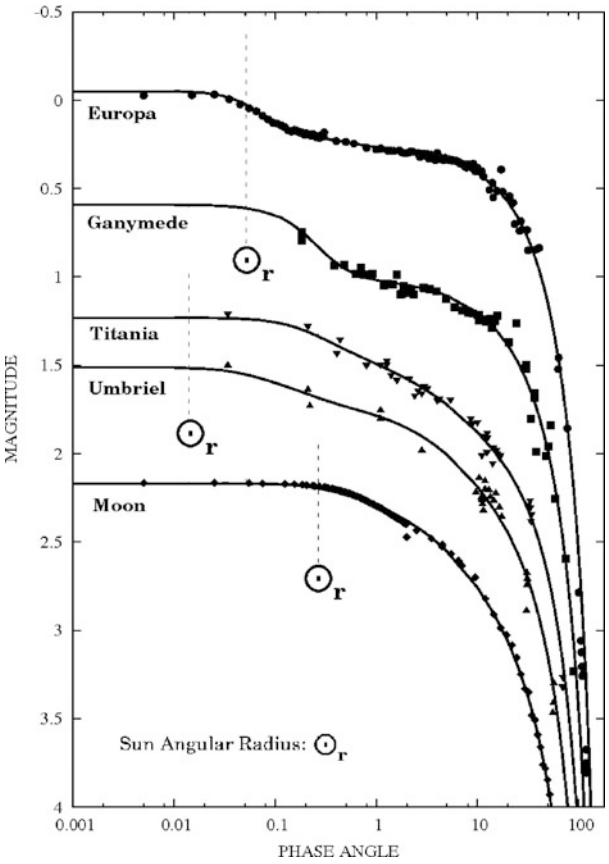

Fig. 2.4 Fits of the Shkuratov-Helfenstein model (Table 2.3) to five objects that have different albedos. Details of fits to the opposition effect are shown (note logarithmic scale for phase angle). Good fits to the opposition effect portion of each phase curve were achieved in all cases. Phase curves and fits plotted to large phase angles show that the model seldom fits well at phase angles larger than 90°. Plots adapted from Helfenstein and Shkuratov (in preparation)

Table 2.3 Example values of Shkuratov-Helfenstein model parameters for selected objects[a]

Object	ω_o	h_{sh}	L	η	(g_1, g_2, f)
Shkuratov and Helfenstein (2001)					
Moon	0.66	0.05	25	1.50	0,0,0
Titania	0.85	0.05	69	0.56	0,0,0
Helfenstein and Shkuratov (2011)					
Moon	0.633	0.077	12	1.18	$0, -0.995, 1.0 \times 10^{-6}$
Umbriel	0.881	0.065	100	0.93	$0, -0.995, 1.0 \times 10^{-5}$
Titania	0.913	0.101	6.8	0.43	$0, -0.995, 1.0 \times 10^{-5}$
Ganymede	>0.999998	0.243	2414	0.35	$0, -0.995, 1.0 \times 10^{-5}$
Europa	>0.999998	0.507	12	0.34	$0, -0.999, 2.5 \times 10^{-7}$

[a]Adapted from Helfenstein and Shkuratov (in preparation)

non-isotropic[3] (Helfenstein and Shepard, in preparation). These improvements were especially needed to obtain good fits to Europa's phase curve. Unfortunately, this approach introduced ambiguity between what portion of the CBOE is due to scattering in the aggregate and what part is intrinsic to the elemental scatterers.

Table 2.2 indicates that the elemental scatterers have relatively large values of ω_o even for dark objects like the Moon and Umbriel, although they are systematically lower than for the brighter icy satellites (Titania, Ganymede, and Europa). Values of the fractal parameter η are near or greater than unity for the darkest objects (the Moon and Umbriel) implying opaque, complexly structured aggregates. In contrast, for the bright icy satellites (Europa, Ganymede, Titania), η is significantly less than unity, implying that the bright icy aggregates are not large or structurally complex enough to become completely opaque. The angular width of the SHOE systematically gets wider for brighter objects than for darker ones. A naïve interpretation would be that regoliths on brighter icy objects are systematically more compacted than on low-albedo bodies. However, a more plausible explanation is that the much greater amount of multiply-scattered light in high-albedo regoliths mutes or renders undetectable the SHOE, except perhaps at very large size scales where surface structures can become opaque. There appears to be no clear systematic dependence of L on regolith type. This differs from results in Shkuratov et al. (1999) and Shkuratov and Helfenstein (2001), where L in general, is found to be systematically longer for brighter objects than for darker objects (presumably because bright relatively transparent ice grains are generally more permeable to photons than dark absorbing ones). However, in the new fits in Table 2.2, the result is likely due to ambiguities resulting both from allowing elemental scatterers to exhibit their own opposition surges and the limited ability to detect the SHOE on bright objects.

2.4 Implications for Planetary Science

Given the recent challenges to the utility of photometry as a tool to discern actual physical surface properties, what can we learn about icy surfaces from the application of the best available photometric models? We can assess the populations of icy bodies in the Solar System in terms of the albedo, color, and phase function and connect these fundamental physical properties to their thermal and weathering histories. Impacts with dusty ring particles serve to enhance the phase functions of the saturnian satellites, yet the process by which the uranian satellite phase functions are enhanced is not known. Do the major satellites of Uranus reside within a tenuous, dark ring? Ejecta exchange between binary (or more) TNO

[3] Helfenstein and Shkuratov's (in preparation) fits from Table 2.3 use a 3THG function for the elemental scatterers, modeling scatterers that are almost entirely isotropic (g_1=0), with only a small fraction (1×10^{-7}–1×10^{-5}) contributed from a non-isotropic extremely narrow backscattering spike (i.e. $g_2 \leq -0.995$).

systems may be an alternative mechanism by which phase functions are enhanced (Stern 2009; Rabinowitz et al. 2009). What conclusions can we draw from the fact that several dwarf planets are as bright as the major giant planet satellites and nowhere near as dark as the "typical" residents in the classical Kuiper belt? Do they also have steep phase functions like the giant planet satellites? Only observations at phase angles close to zero will tell; however, node crossings for these bodies do not occur until decades from now.

2.5 Summary and Future Work

Future laboratory work will certainly advance the application of photometric models to observations of icy surfaces in the Solar System. The Hapke (2008) correction for the effects of porosity should follow the preliminary test published by Helfenstein and Shepard (2011).

The successful completion of several upcoming spacecraft missions will supply key observations of icy surfaces not yet seen at spatial resolutions exceeding those attainable by the newly refurbished *Hubble Space Telescope*. Foremost among these are the images anticipated from the *New Horizons* spacecraft as it makes the first reconnaissance of a dwarf planet, Pluto and its satellites Charon, Nix, and Hydra in 2015. Following the Pluto flyby, *New Horizons* plans to target at least one additional Kuiper belt object.

The *Cassini* spacecraft has begun the final phase of its exploration of the Saturn system which will continue until the next Saturn solstice in 2017. To date, the mission has returned hundreds of thousands of images of Saturn's rings and satellites; the "Solstice" mission will add to an already incredibly rich data set, expanding the coverage in illumination and viewing angles across the visible and near-infrared spectrum for the icy surfaces in Saturn's realm.

The Atacama Large Millimeter Array (ALMA) will measure diameters for hundreds of TNOs, making possible determinations of their geometric albedos and ultimately the distribution of mass throughout the Solar System beyond the orbit of Neptune.

References

Bauer J et al (2003) Physical survey of 24 Centaurs with visible photometry. Icarus 166:195

Boehnhardt H et al (2008) Photometry and polarimetry of the nucleus of comet 2P/Encke. Astron Astrophys 489:1337

Brucker MJ et al (2009) High albedos of low inclination classical Kuiper belt objects. Icarus 201:284

Buie MW, Grundy WM, Young EF, Young LA, Stern SA (2010) Pluto and Charon with the Hubble Space Telescope. I. Monitoring global change and improved surface properties from light curves. Astron J 139:1117

Buratti BJ, Veverka J (1985) Photometry of rough planetary surfaces – the role of multiple scattering. Icarus 64:320

Buratti BJ et al (2008) Infrared (0.83 5.1 μm) photometry of Phoebe from the Cassini visual infrared mapping spectrometer. Icarus 193:309
Buratti BJ et al (2011) Photometry of Triton 1992-2004: Surface volatile transport and discovery of a remarkable opposition surge. Icarus 212:835
Chandrasekhar S (1960) Radiative transfer. Dover, New York
Chernova GP, Lupishko DF, Shevchenko VG (1994) Photometry and polarimetry of the asteroid 24 Themis. Kinemat Phys Neb Tel 10:45
Davies JK, McBride N, Ellison SL, Green SF, Ballantyne DR (1998) Visible and infrared photometry of six Centaurs. Icarus 134:213
Domingue D, Verbiscer A (1997) Re-analysis of the solar phase curves of the icy Galilean satellites. Icarus 128:49
Domingue DL, Hapke BW, Lockwood GW, Thompson DT (1991) Europa's phase curve – implications for surface structure. Icarus 90:30
Drossart P (1993) Optics on a fractal surface and the photometry of the regoliths. Plan Space Sci 41:381
Fernandez Y, Sheppard SS, Jewitt DC (2003) The albedo distribution of Jovian Trojan asteroids. Astron J 126:1563
French RG et al (2007) Saturn's rings at true opposition. Pub Astron Soc Pacific 119:623
Gladman B, Marsden BG, Vanlaerhoven C (2008) Nomenclature in the outer solar system. In: Barucci MA et al (eds) University of Arizona Press, Tucson, p 43
Goguen J (1981) A theoretical and experimental investigation of the photometric functions of particulate surfaces. Ph.D. Thesis, Cornell University, Ithaca
Goguen JD, Stone TC, Kieffer HH, Buratti BJ (2010) A new look at photometry of the Moon. Icarus 208:548
Gunderson K, Thomas N, Whitby JA (2006) First measurements with the Physikalisches Institut Radiometric Experiment (PHIRE). Plan Space Sci 54:1046
Hapke B (1981) Bidirectional reflectance spectroscopy. 1. Theory. J Geophys Res 86:565
Hapke B (1984) Bidirectional reflectance spectroscopy. III – Correction for macroscopic roughness. Icarus 59:41
Hapke B (1986) Bidirectional reflectance spectroscopy. IV – The extinction coefficient and the opposition effect. Icarus 67:264
Hapke B (1990) Coherent backscatter and the radar characteristics of outer planet satellites. Icarus 88:407
Hapke B (1993) Theory of reflectance and emittance spectroscopy. Cambridge University Press, New York
Hapke B (2002) Bidirectional reflectance spectroscopy. 5. The coherent backscatter opposition effect and anisotropic scattering. Icarus 157:523
Hapke B (2008) Bidirectional reflectance spectroscopy. 6. Effects of porosity. Icarus 195:918
Hapke BW, Nelson RM, Smythe WD (1993) The opposition effect of the moon – the contribution of coherent backscatter. Science 260:509
Hapke B, Nelson R, Smythe W (1998) The opposition effect of the Moon: coherent backscatter and shadow hiding. Icarus 133:89
Hapke B, Shepard MK, Nelson RM, Smythe W, Piatek J (2009) A quantitative test of the ability of models based on the equation of radiative transfer to predict the bidirectional reflectance of a well-characterized medium. Icarus 199:210
Harris AW et al (1989) Photoelectric observations of asteroids 3, 24, 60, 261, and 863. Icarus 77:171
Helfenstein P (1986) Derivation and analysis of geological constraints on the emplacement and evolution of terrains on Ganymede from applied differential photometry. PhD thesis, Brown University, Providence
Helfenstein P (1988) The geological interpretation of photometric surface roughness. Icarus 73:462
Helfenstein P, Shepard MK (1999) Submillimeter-scale topography of the lunar regolith. Icarus 141:107
Helfenstein P, Shepard MK (2011) Testing the Hapke photometric model: Improved inversion and the porosity correction. Icarus 215:83

Helfenstein P, Veverka J, Thomas PC (1988) Uranus satellites – Hapke parameters from Voyager disk-integrated photometry. Icarus 74:231
Helfenstein P, Veverka J, Hillier J (1997) The lunar opposition effect: a test of alternative models. Icarus 128:2
Henyey C, Greenstein J (1941) Diffuse radiation in the galaxy. Ap J 93:70
Hillier J et al (1990) Voyager disk-integrated photometry of Triton. Science 250:419
Howett CJA, Spencer JR, Pearl JC, Segura ME (2010) Thermal inertia and bolometric Bond albedo values for Mimas, Enceladus, Tethys, Dione, Rhea and Iapetus as derived from Cassini/CIRS measurements. Icarus 206:573
Irvine WM (1966) The shadowing effect in diffuse reflection. J Geophys Res 71:2931
Kaasalainen S et al (2003) Asteroid photometric and polarimetric phase curves: empirical interpretation. Icarus 161:34
Karkoschka E (2001) Comprehensive photometry of the rings and 16 satellites of Uranus with the Hubble Space Telescope. Icarus 151:51
Kattawar GW (1975) A three-parameter analytic phase function for multiple scattering calculations. J Quan Spectr Rad Trans 15:839
Lambert JH (1760) Photometria. W. Engelmann, Leipzig
Lazzaro D et al (1997) Photometric monitoring of 2060 Chiron's brightness at perihelion. Plan Space Sci 45:1607
Lebofsky LA, Spencer JR (1989) Systematic biases in radiometric diameter determinations. In: Binzel RP et al (eds) Asteroids II. University of Arizona Press, Tucson, p 128
Li J-Y et al (2007a) Deep Impact photometry of Comet 9P/Tempel 1. Icarus 187:41
Li J-Y, A'Hearn MF, McFadden LA, Belton MJS (2007b) Photometric analysis and disk-resolved thermal modeling of Comet 19P/Borrelly from Deep Space 1 data. Icarus 188:195
Li J-Y, A'Hearn MF, Farnham TL, McFadden LA (2009) Photometric analysis of the nucleus of Comet 81P/Wild 2 from Stardust images. Icarus 204:209
Lumme K, Bowell E (1981) Radiative transfer in the surfaces of atmosphere less bodies. I – Theory. II – Interpretation of phase curves. Astron J 86:1694
Lumme K, Bowell E (1985) Photometric properties of zodiacal light particles. Icarus 62:54
Luu J, Jewitt D (1996) Color diversity among the Centaurs and Kuiper belt objects. Astron J 112:2310
McGuire A, Hapke B (1995) An experimental study of light scattering by large, irregular particles. Icarus 113:134
Miller C, Verbiscer AJ, Chanover N, Holtzman J, Helfenstein P (2011) Comparing Phoebe's 2005 opposition surge in four visible light filters. Icarus 212:819
Minnaert M (1941) The reciprocity principle in lunar photometry. Ap J 93:403
Mishchenko MI (1992) The angular width of the coherent back-scatter opposition effect - an application to icy outer planet satellites. Astrophys Space Sci 194:327
Muinonen K (1990) Light scattering by inhomogeneous media: backward enhancement and reversal of linear polarization. PhD thesis, Helsinki University, Helsinki
Müller TG et al (2010) "TNOs are cool": A survey of the trans-Neptunian region. I. Results from the Herschel science demonstration phase (SDP). Astron Astrophys 518:146
Ozrin VD (1992) Exact solution for coherent backscattering of polarized light from a random medium of Rayleigh scatterers. Waves Random Med 2:141
Paranicas C, Cooper JF, Garrett HB, Johnson RE, Sturner SJ (2009) Europa's radiation environment and its effects on the surface. In: Pappalardo RT et al (eds) Europa. University of Arizona Press, Tucson, p 529
Piatek J, Hapke BW, Nelson RM, Smythe WD, Hale AS (2004) Scattering properties of planetary regolith analogs. Icarus 171:531
Pitman KM, Buratti BJ, Mosher JA (2010) Disk-integrated bolometric Bond albedos and rotational light curves of Saturnian satellites from Cassini Visual and Infrared Mapping Spectrometer. Icarus 206:537
Rabinowitz DL et al (2006) Photometric observations constraining the size, shape, and albedo of 2003 EL61, a rapidly rotating, Pluto-sized object in the Kuiper belt. Ap J 639:1238

Rabinowitz DL, Schaefer BE, Tourtellotte SW (2007) The diverse solar phase curves of distant icy bodies. I. Photometric observations of 18 trans-Neptunian objects, 7 Centaurs, and Nereid. Astron J 133:26
Rabinowitz DL, Schaefer B, Schaefer M, Tourtellotte S (2009) Evidence for recent resurfacing of the binary Kuiper belt object 1997 CS29. BAAS 41:6509
Rousselot P, Petit JM, Poulet F, Sergeev A (2005) Photometric study of Centaur (60558) 2000 EC98 and trans-Neptunian object (55637) 2002 UX25 at different phase angles. Icarus 176:478
Schaefer BE, Tourtellotte SW, Rabinowitz DL, Schaefer MW (2008) Nereid: Light curve for 1999 2006 and a scenario for its variations. Icarus 196:225
Schaefer MW, Schaefer BE, Rabinowitz DL, Tourtellotte SW (2010) Phase curves of nine Trojan asteroids over a wide range of phase angles. Icarus 207:699
Shepard MK, Campbell BA (1998) Shadows on a planetary surface and implications for photometric roughness. Icarus 134:279
Shepard MK, Helfenstein P (2007) A test of the Hapke photometric model. J Geophys Res 112: E03001
Shevchenko VG et al (2009) Do Trojan asteroids have the brightness opposition effect? Lunar Plan Sci Conf 40:1391
Shkuratov YG (1988) A diffraction mechanism for the formation of the opposition effect of the brightness of surfaces having a complex structure. Kinemat Phys Neb Tel 4:33
Shkuratov Y, Helfenstein P (2001) The opposition effect and the quasi-fractal structure of regolith: I. Theory. Icarus 152:96
Shkuratov Y et al (1991) A possible interpretation of bright features on the surface of Phobos. Plan Space Sci 39:341
Shkuratov Y, Starukhina L, Hoffman H, Arnold G (1999) A model of spectral albedo of particulate surfaces: implications for optical properties of the Moon. Icarus 137:235
Shkuratov Y et al (2007) Photometry and polarimetry of particulate surfaces and aerosol particles over a wide range of phase angles. J Quan Spectr Rad Trans 106:487
Sicardy B et al (2011) A Pluto-like radius and a high albedo for the dwarf planet Eris from an occultation. Nature 478:493
Soderblom LA et al (1990) Triton's geyser-like plumes – discovery and basic characterization. Science 250:410
Souchon A et al (2011) An experimental study of Hapke's modeling of natural granular surface samples. Icarus 215:313
Spencer JR (1987) Thermal segregation of water ice on the Galilean satellites. Icarus 69:297
Spencer JR et al (2006) Cassini encounters Enceladus: background and the discovery of a south polar hot spot. Science 311:1401
Stansberry J et al (2008) Physical properties of Kuiper belt and Centaur objects: constraints from the Spitzer Space Telescope. In: Barucci MA et al (eds) The solar system beyond Neptune. University of Arizona Press, Tucson, p 592
Stern SA (2009) Ejecta exchange and satellite color evolution in the Pluto system, with implications for KBOs and asteroids with satellites. Icarus 199:571
Verbiscer A (1991) Photometry of icy satellite surfaces, Ph.D. Thesis, Cornell University, Ithaca
Verbiscer A, Helfenstein P (1998) Reflectance spectroscopy of icy surfaces. In: Schmitt B et al (eds) Solar system ices. Kluwer, Dordrecht, p 157
Verbiscer A, Veverka J (1989) Albedo dichotomy of Rhea – Hapke analysis of Voyager photometry. Icarus 82:336
Verbiscer A, Veverka J (1992) Mimas – photometric roughness and albedo map. Icarus 99:63
Verbiscer A, Veverka J (1994) A photometric study of Enceladus. Icarus 110:115
Verbiscer A, Helfenstein P, Veverka J (1990) Backscattering from frost on icy satellites in the outer solar system. Nature 347:162
Verbiscer A, French RG, Showalter M, Helfenstein P (2007) Enceladus: Cosmic graffiti artist caught in the act. Science 315:815
Verbiscer AJ, Skrutskie MF, Hamilton DP (2009) Saturn's largest ring. Nature 461:1098
Verbiscer AJ, Fisher TM, French RG (2010) The strongest opposition surges: products of ejecta exchange? BAAS 42:957

http://www.springer.com/978-1-4614-3075-9

The Science of Solar System Ices
Gudipati, M.S.; Castillo-Rogez, J. (Eds.)
2013, XIV, 658 p., Hardcover
ISBN: 978-1-4614-3075-9